Crustal heterogeneity of Antarctica signals spatially variable radiogenic heat production

L. Li[1], A.R.A. Aitken[1,2]

[1] School of Earth Sciences, The University of Western Australia, Perth, Western Australia, Australia.

[2] Australian Centre of Excellence for Antarctic Science, The University of Western Australia, Perth, Western Australia, Australia

Corresponding author: Lu Li (lu.li@uwa.edu.au)

Key Points:

- Antarctic crustal model is derived by seismic-constrained gravity inversion.
- Variable crustal radiogenic heat production is inferred from crustal density and petrophysical data.
- The impact of heterogeneity in crustal heat production for geothermal heat flow is quantified.

Abstract

Crustal structure controls geothermal heat flux which is a key basal boundary conditions for ice-sheet flow in Antarctica. The crustal thickness of Antarctica is well resolved at large-scale, but the smaller-scale structures and density variations in the crust remain poorly constrained. Using 3D gravity inversion constrained by seismic Moho estimates, we model crustal structure in Antarctica, resolving sedimentary basin thickness and density, crustal density and internal layering, and the Moho. Spatial variations in upper crustal density are mapped to radiogenic heat production using a petrophysically-defined mapping approach. Significant variations are observed averaging 1.2 to 1.6 μW/m^3, and as high as 2 μW/m^3 in West Antarctica. The crustal contribution to geothermal heat flow is similarly variable averaging 18 to 27 mW/m^2 and could be up to 60 mW/m^2. The mapped variations are significant for correctly representing heat flow in Antarctica.

Plain Language Summary

The structure of Antarctica's crust—including sedimentary basins, the density of igneous and metamorphic crust, and the interface between the crust and mantle—drives the delivery of heat to the ice sheet's base with capacity to influence ice sheet flow. However, these structures are not well-understood due to the extensive and thick ice cover combined with limited geophysical observations. By examining anomalies in the Earth's gravity field and using independent depth constraints from seismic studies, we investigate the variations in crustal geometry and density. Our findings indicate that the heterogeneous crustal structure results in variable heat production within the crust, influencing the heating of the ice sheet's base to a significant degree, including several areas with more heat than previously estimated.

1. Introduction

To make accurate predictions of the future behaviour of the Antarctic Ice Sheet demands understanding the subglacial boundary conditions, in particular geothermal heat flow (GHF), variations in which may be important drivers of variable ice sheet dynamics (McCormack et al., 2022). Elevated GHF may promote enhanced basal melting and influence the rheology of the ice sheet, thus directly controlling its overall flow (Noble et al., 2020).

The inaccessibility of the ice sheet bed has limited direct observations of GHF and large-scale understanding relies heavily on models derived from geophysical data (e.g., An et al. (2015b)). Spatially variable heat flow for Antarctica has been estimated in the past using magnetic and seismic methods (An et al., 2015b; Martos et al., 2017). These methods characterize the thermal structure of the lithosphere by the geometry of a single inferred boundary either the Curie isotherm (580°C) or lithosphere-asthenosphere boundary isotherm (1300°C). GHF is calculated from the thermal gradient between the isotherm and the ice sheet bed using typical lithospheric thermal properties.

A limitation of these approaches is the neglecting the effects of radiogenic heat production, which locally can account for up to 70% of heat flow (Burton-Johnson et al., 2017), and may vary significantly on small length-scales. Averages derived from large-scale geophysical models will fail to represent more local variations well and yet these are critical for controlling ice sheet dynamics (McCormack et al., 2022).

More recent geothermal heat flow models have started to incorporate heterogeneity using statistical methods and multi-geophysical data (Lösing & Ebbing, 2021; Lösing et al., 2020; Shen et al., 2020; Stål et al., 2020; Stål et al., 2021). Different models are converging (Reading et al., 2022), however, the uncertainties in input variables are known to significantly impact the results of statistical models. This is likely the case in Antarctica, where first-order solid-earth structures are constrained by sparse seismic estimates. In addition, there is generally a large uncertainty in areas without constraints, as well as a lack of understanding of the internal variability of the crust.

In Antarctica, both seismic and gravity applications resolve substantial regional variations in crust and mantle structure (Abrehdary & Sjöberg, 2021; Haeger & Kaban, 2019; Haeger et al., 2019; Lloyd et al., 2020; Pappa et al., 2019a; Pappa et al., 2019b). Studies of Antarctic crustal structure have mainly focused on the interface between crust and mantle (marked by Moho discontinuity). This interface is primarily constrained by receiver function analysis (Baranov & Morelli, 2013; Chaput et al., 2014; Dunham et al., 2020; Hansen et al., 2009) and tomography models (An et al., 2015a; Shen et al., 2018). Recent applications have also begun to resolve structure within the crust (Zhou et al., 2022). However, due to the challenging fieldwork environment, seismic observations are sparse and have uneven spatial coverage, which limits their ability to resolve crustal structures in detail.

Benefiting from the broader spatial coverage of gravity measurement, gravity inversion is an alternative approach to estimate the Moho undulations, variably constrained by seismic information (Chisenga et al., 2019; Llubes et al., 2018; Pappa et al., 2019a; Zhang et al., 2020). These studies assume that long-wavelength Bouguer gravity reflects Moho undulations and use geometry inversion techniques with a single density contrast to recover the Moho. However, this assumption is problematic in continental-scale applications due to lateral variations in crust and mantle density structure that can generate gravity anomalies of comparable magnitude to the Moho as well as affecting density contrast across the interface (Aitken, 2010; Aitken et al., 2013).

An alternative approach involves incorporating all critical surfaces and density structures as updatable features within a single model domain. A 3D gravity inversion is then utilized to determine the optimal density and geometry (Aitken, 2010; Aitken et al., 2013; Alghamdi et al., 2018). This approach accounts for a laterally heterogeneous crust and mantle with the capability to generate seismic-constrained Moho and density structure in a continental-scale application (Aitken, 2010; Aitken et al., 2013).

Here, we build a 3D model domain including sedimentary basin, upper and lower crust layers and mantle. During the inversion, the density and thickness of each layer are modified within seismic constraints and density bounds, and with differing constraints applied to the solution. An ensemble of results is assembled that fits both the gravity observations and the prior seismic constraints. The ensemble result presents the most representative model of Antarctic crustal structure possible within the capacity of the method and current data constraints. From the ensemble result, we explore the implications of heterogeneity in crustal structure for radiogenic heat production and GHF in Antarctica.

2. Data and methods

2.1 Free-air gravity data

In our inversion, we invert free-air gravity data. For the dataset, airborne gravity datasets (the AntGG compilation (Scheinert et al., 2016) and regional-scale free-air gravity data, Supporting Information Text S1) are combined with the GOCO06s satellite gravity model (Kvas et al., 2019) calculated at 5 km ellipsoid height (Figure 1a). After merging, the long-wavelength gravity information predominantly caused by the mantle convection or sub-lithospheric mantle density variations was removed using the spherical harmonics 0 to 10 degree (approximately > 2000 km half-wavelength) from GOCO06s model.

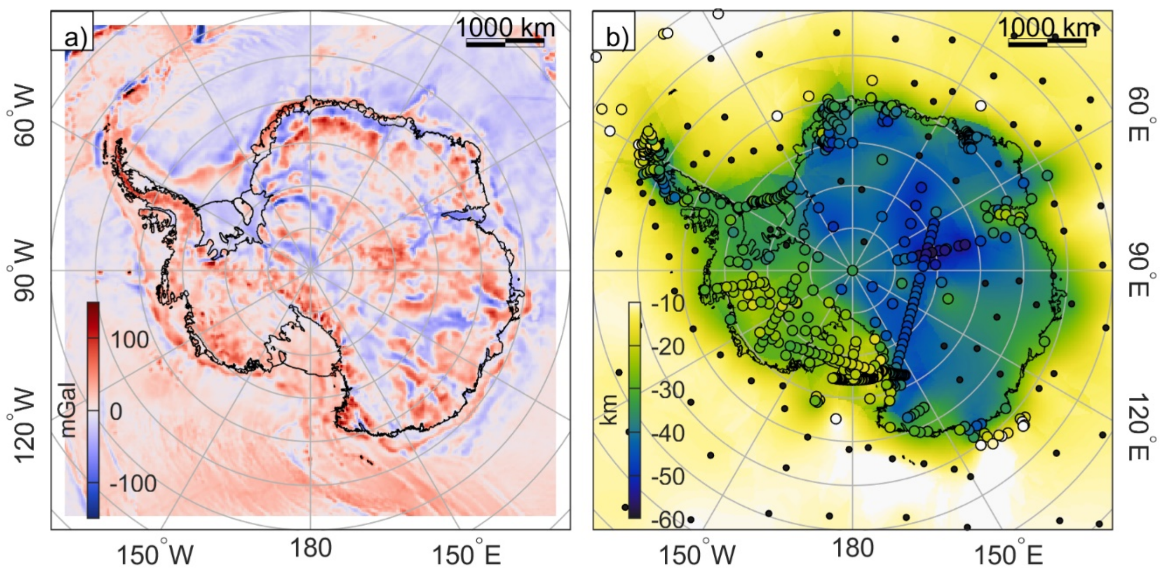

Figure 1. a) Free-air gravity data from airborne gravity measurements and satellite gravity model GOCO6S. The long-wavelength gravity is removed. b) Initial Moho surface generated from seismic Moho and isostatic Moho using Kriging. Coloured dots show the seismic Moho constraints, and black dots show arbitrarily located control points.

2.2 Initial model

The initial model incorporates the current understanding of Antarctic crustal structure by including the results of recent seismic studies (see An et al. (2015a) and Supporting Information Table S2). The model domain has a horizontal grid resolution of 20 km and extends to a depth of 75 km. It is divided into nine layers, including ice, lake water, seawater, sedimentary basins (with three layers accounting for sediment compaction with depth), crystalline crust (upper and lower crust), and mantle. The initial and permitted density ranges for each layer are shown in Supporting Information Table S1. We use the BedMachine Antarctica (Morlighem et al., 2020) to represent the topographic components of the model (ice surface and bed topography and lake and ocean bathymetry). The mean value of topography values in the 20 km cell size is used to conserve the mass of topography components and avoid misrepresentation of localised topography.

Sedimentary basins have a significant impact on gravity due to their high density contrast and proximity to observation locations. To represent offshore sedimentary cover and thickness, we use the GlobSed dataset (Straume et al., 2019) with the exception of major ice shelf regions (Ross Ice Shelf and Filchner-Ronne Ice Shelf), where sedimentary basin thickness is estimated from depth to magnetic basement (Golynsky et al., 2006; Tankersley et al., 2022). Onshore, sedimentary basin distribution and thickness are not well-constrained. Li et al. (2022) utilized a machine learning method to map sedimentary basin distribution as a likelihood, which for the initial model was scaled into a sedimentary basin thickness map (Supporting Information Text S2) using a relationship between sedimentary basin thickness and likelihood derived from four sedimentary basin estimations in Ross Ice Shelf (Tankersley et al., 2022), the Wilkes Subglacial Basin (Frederick et al., 2016) and Wilkes Land (Aitken et al., 2016; Maritati et al., 2016).

We define the initial Moho surface and its uncertainty based on the kriging prediction and error using individual Moho estimates from receiver function analyses (see Figure 2). For areas more than 200 km distant from seismic observation, we use a local Airy isostatic model based on the rock equivalent topography from BedMachine Antarctica (Morlighem et al., 2020). For these estimates, a reference 35 km Moho depth and 0.625 kg/m^3 density contrast were used, as these values are suggested to best fit the seismic measurements in East Antarctica (Pappa et al., 2019a). In the offshore region without seismic estimation across continental shelf, we use a uniform 7 km thick oceanic crust. We use the prediction error from kriging to represent the upper and lower bound of permissible Moho surface elevation (± 2 Standard Deviation (STD)). The unconstrained area has a uniform uncertainty of ± 5 km. In the crust, a two-layer crust with upper and lower crust layers of equal thickness is used in the continental crust and a single-layer dense crust is used in the oceanic crust.

2.3 Gravity inversion

3D gravity inversions were undertaken using VPMG software (Fullagar et al., 2008), which divides the model domain with prism-elements of pre-defined area with arbitrary thickness. VPMG has two main gravity inversion styles: density-style, where the densities of prism-elements are varied, and geometry-style, where the elevations of the prism-element boundaries are modified. Each style works independently, and the other property cannot change. VPMG has the capacity to locally allow change or set constraints on geometry and density during the inversion process. Due to their relatively high confidence, the geometries of the surfaces defining the ice surface, Lake Vostok, bed topography/bathymetry and the base of the offshore sedimentary basins were completely fixed during the inversion. The sedimentary basin thickness is permitted to change in areas with sedimentary basin likelihood higher than 0.4, while areas with sedimentary basin likelihood less than 0.4 indicate a crystalline basement dominant region and are fixed with 0 thickness in the inversion. The Moho surface is allowed to change within the upper and lower bounds as described in Section 2.2.

This study followed the alternating inversion method used by (Aitken et al., 2013; Alghamdi et al., 2018). In this approach, a density-style inversion and a geometry-style inversion are alternated and repeated for a number of cycles. In each inversion cycle, we apply four inversions. First, we solve one iteration for mantle density, then one iteration each for the density within the crust layers, the geometry of the Moho, and the sedimentary basin thickness. The inversion cycle is run three times for a total of 12 iterations. The inversion process is regulated by the maximum permitted change in each style: for a density style inversion, the permitted change is the absolute density allowance in the current iteration; for a geometry style inversion, the permitted change is set as the percentage of the interface elevation change compared with the initial elevation. Increasing permitted changes allows more change to be accommodated in that phase, which increases the capacity to resolve misfit. Setting the range of permitted changes allows us to control how the inversion is solved.

In total 35 inversions were run to generate a model-ensemble each containing results constrained by different permitted density or geometry changes. The permitted density change in each iteration ranged from 5 kg/m^3 to 40 kg/m^3 by 5 kg/m^3 intervals while geometry change ranged from 5% to 13% by 2% intervals, respectively (Supporting Information Figure S5). After the model selection, we use the mean of the model-ensemble and its standard deviation to show a representative crustal structure (Supporting Information Text S3).

3. Results

Our model-ensemble results indicate spatial variations in sedimentary layer thickness beneath the ice sheet and ice shelf (Figure 2a). We have resolved a sedimentary layer with average 1 km thickness in onshore West Antarctica where sedimentary basin is present. These results are consistent with passive seismic estimations (Chaput et al., 2014; Dunham et al., 2020; Zhou et al., 2022). In contrast, the East Antarctica section preserves thicker sedimentary packages, with an average thickness of 2 km. Major and thick sedimentary basins (3-4 km) are preserved in the Aurora Subglacial Basin and Pensacola Pole Basin. The Wilkes Subglacial Basin is thinner (1-2 km) in the north, with a thicker basin in the south (3-4 km). Thick sedimentary basins are identified beneath major ice shelves, with a thickness of 8-12 km resolved in the Filchner-Ronne Ice Shelf (FRIS). The basin is thickest closest to the edge of the ice shelf and becomes thinner towards the western side of the inner ice shelf. For the Ross Ice Shelf (RIS), we have resolved near 1-3 km of sediment that is thicker from the grounding line to the edge of the ice shelf into the Ross Sea. The western side of the RIS is generally thicker than the eastern side, separated by a mid-shelf high (Tankersley et al., 2022). The sedimentary basin beneath the Amery Ice Shelf is narrower, with a thickness of 3 km.

The thinner crust in West Antarctica (25 km) and thicker crust in East Antarctica (35 km) are captured by the mean Moho as shown in Figure 2b and Supporting Information Figure S5b. The thinnest crust occurs in the Ross Sea, Byrd Subglacial Basin, and Byrd Subglacial Trench as part of the West Antarctic Rift System (WARS), while the thickest crust occurs beneath the Gamburtsev Subglacial Mountains (GSM). The STD of the Moho surface shows variability within the model-ensemble, as seen in Supporting Information Figure S6. This variability reflects both the consistency of the initial model with the gravity field and the influence of the applied constraints. High STD occurs where constraints are weak, and the initial model does not explain gravity observations. Conversely, low STD occurs where either constraint is strong or the initial model is already explaining gravity observations. For instance, in the GSM region, we see that the deep Moho, constrained by seismic data (Hansen et al., 2010) shows a large variance after inversion. This large Moho variation indicates that the initial Moho does not match gravity observation, which requires either reducing the crust thickness (Pappa et al., 2019a) or including a dense mafic underplate structure (Ferraccioli et al., 2011). In the Wilkes Land region, the Moho shows low variance despite low seismic data constraints. This indicates that the initial isostatic assumption is close to matching the gravity observation.

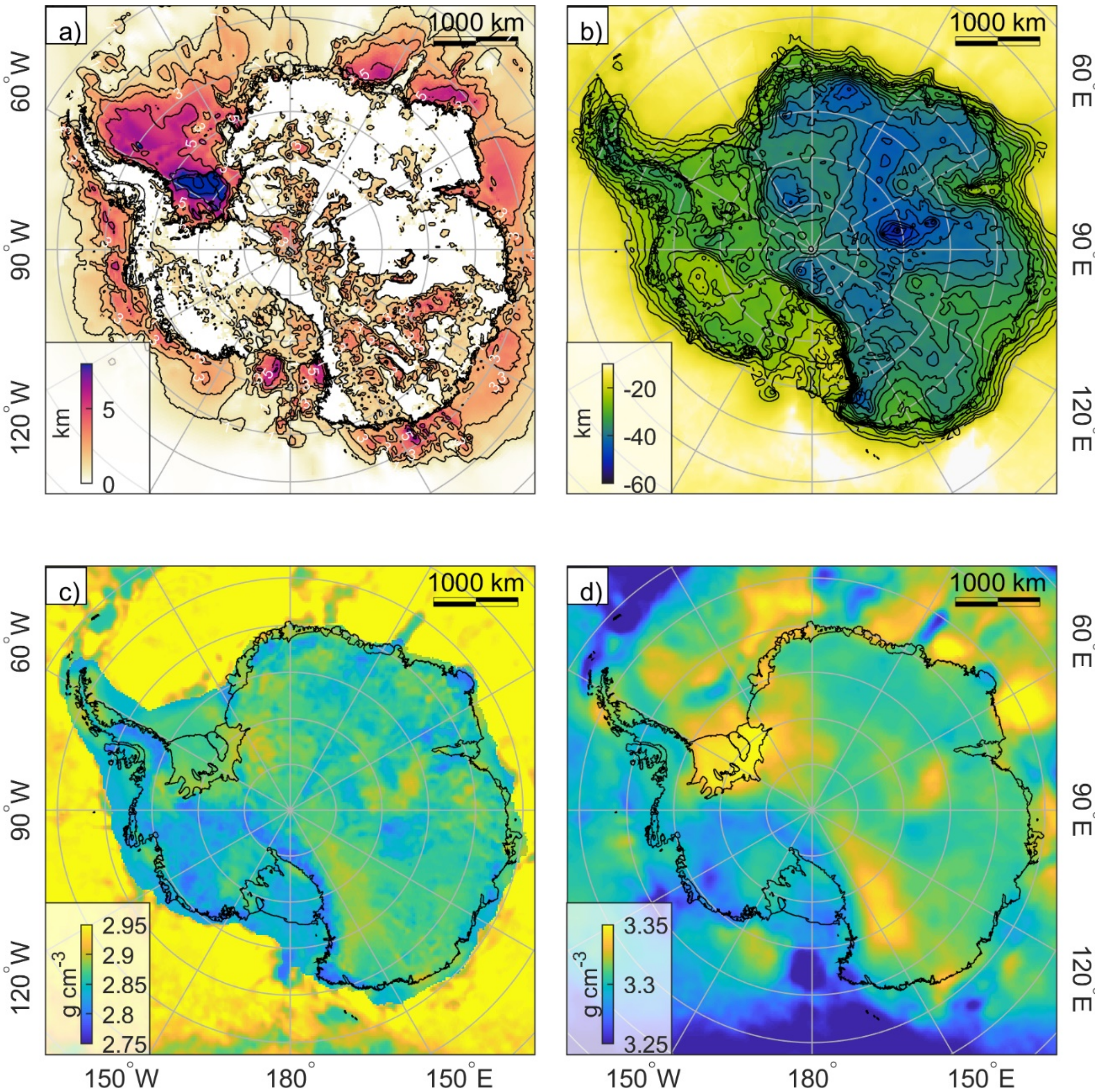

Figure 2. The model-ensemble mean result. a) sedimentary basin thickness; b) Moho depth; c) crystalline crust density; d) mantle density

4. Discussion

4.1 Model limitations and value

At continental-scale, gravity inversion has low sensitivity to the depth of anomaly sources. Residual gravity anomalies longer than 400 km in wavelength (5 times model vertical extension) are effectively indistinguishable from a 1D response, meaning that the depth of the sources of these anomalies is undefined. The low vertical sensitivity might account for the similar structure observed for both the mantle and crustal density. Our model sensitivity test indicates that, given the current constraints, changing the mantle density alone is insufficient to account for the residual gravity anomaly (Supporting Information Figure S4a). On the other hand, crustal density has the power necessary to explain all onshore residual gravity anomalies (Supporting Information Figure S4c). In this situation, the crustal anomaly could be up to 50%

greater than the model-ensemble mean. However, a homogenous mantle is unlikely where seismic tomography models reveal large lateral variations in the upper mantle (An et al., 2015a; Lloyd et al., 2020; Shen et al., 2018).

The most robust constraint in our model is the Moho measurement. The model-ensemble mean Moho depth is close to the seismic Moho estimations with an RMS misfit of 3.8 km. This misfit falls within the uncertainty range of 3-5 km from receiver function studies (Supporting Information Figure S7), which is lower than the RMS misfit of other continental-scale models (e.g. 6.9 km in Pappa et al. (2019b), 6.2 km in Zhang et al. (2020)). Although constraints do not exist for the density distribution in the crust and mantle, the mantle density derived from model-ensemble mean exhibits a similar structure to the average mantle Vs (50 km beneath Moho) obtained from Bayesian inversion of Rayleigh wave and receiver functions (Shen et al., 2018).

4.2 Geothermal heat flow due to variable heat production

4.2.1 Crustal heat production estimation

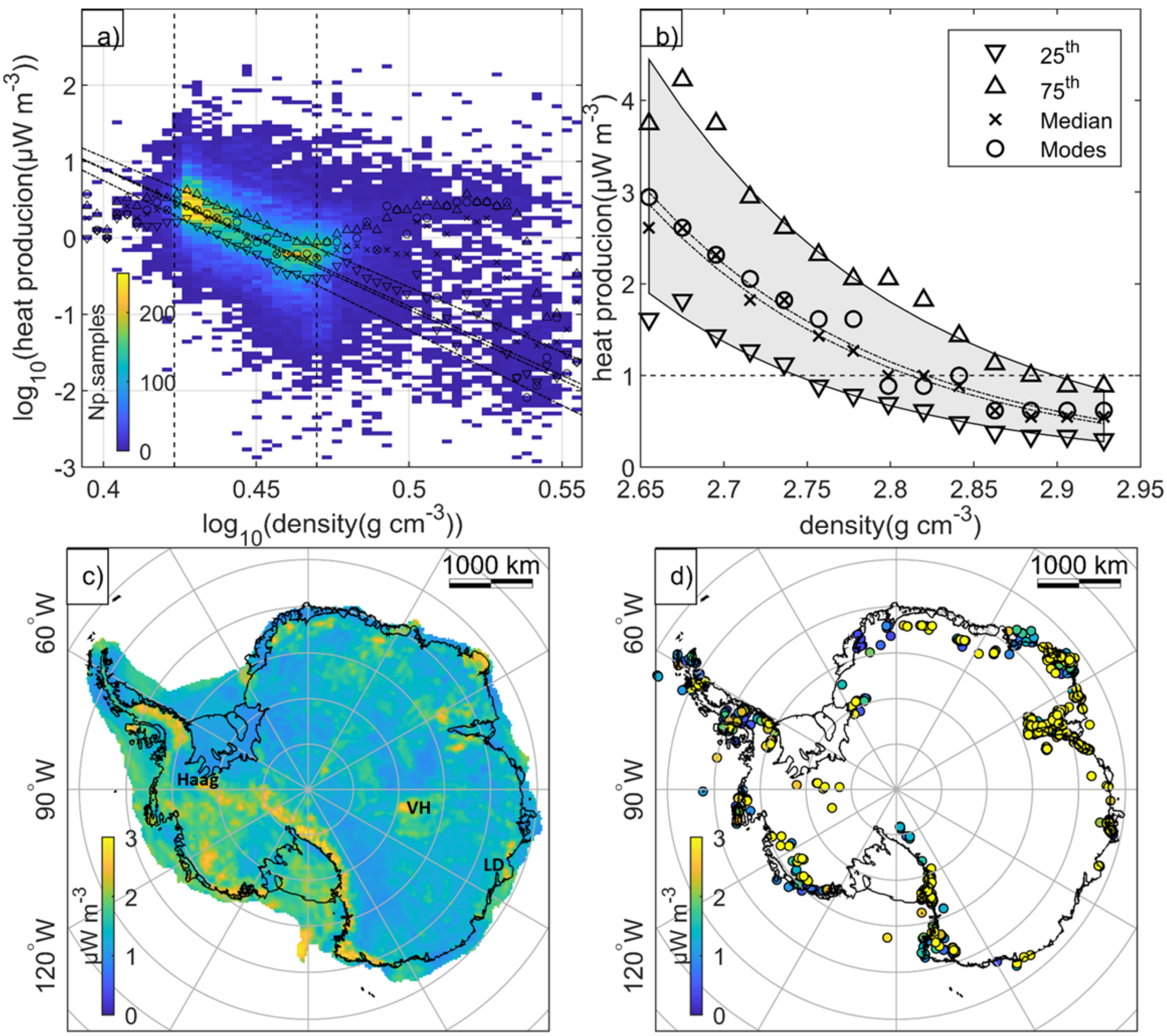

Figure 3. a) 2D histogram of density and heat production in $\log_{10}$ space; b) linear regression of density and heat production, with the shaded area showing the fitted heat production values using the 25th and 75th percentile of heat production value for each density bin; the cross and circle show the median and mode of heat production values for each density bin, respectively, and the density extension is set with the dashed-line range in panel (a) ; c) Modelled heat production map based on the mode fitting; d) PetroChron Antarctica dataset (Sanchez et al., 2021). El, Enderby Land; LD, Lawn Dome; VH, Vostok Highland. Colormap is truncated at 3 $\mu W/m^3$.

Using the global whole-rock geochemical database (Gard et al., 2019) (Figure 3a-b, Supporting Information Test S4), we estimated the statistical relationship between rock density and heat production. Applying this relationship to our modelled upper crust density, we generated an upper crust heat production map (Figure 3c). The map shows that West Antarctica generally has higher heat production than East Antarctica, with major areas exhibiting heat production higher than 1.8 $\mu W/m^3$, except for the ridge of the WARS and the Haag block with heat production less than 1.4 $\mu W/m^3$. East Antarctica shows lower heat production, with an average of 1.2 $\mu W/m^3$, while local areas such as Law Dome, Enderby Land, Vostok highland, and the DML region have elevated heat production higher than 2 $\mu W/m^3$. On the other hand, GSM and the southern Wilkes Subglacial Basin exhibit low heat production, less than 1 $\mu W/m^3$.

4.2.2 Heat production model validation

To date, there is no continental scale heat production map available in Antarctica. In order to validate our model, we compared our heat production map with the PetroChron Antarctica dataset (Sanchez et al. (2021), Figure 3d). Our model shows a good match with the long wavelength information from the database, with elevated heat production in areas such as Antarctica Peninsula, TAM, Enderby Land, and Lambert Rift well captured by our model. Our model also indicates low heat production values in the coastal region of East Antarctica. For a quantitative analysis, the misfit between the modeled heat production, with both the mean and STD, is presented in the Supporting Information Figure S9. A consistent result is shown in the statistical analysis (mean value = 0.61 $\mu W/m^3$, STD = 0.86 $\mu W/m^3$) for both models.

4.2.3 Implication for radiogenic crust contribution for geothermal heat flow

We calculated the contribution of radiogenic heat production from the crust to the total heat flow by using the estimated heat production value (Figure 4c) and the upper crust thickness (Figure 4b). Our findings suggest that radiogenic heat production could contribute up to 50 mW/m^2 to heat flow. Areas with thick crust and high heat production show a greater crustal contribution. In specific regions such as Lambert, DML, and Vostok, the crustal heat production could contribute to heat flows exceeding 40 mW/m^2 (Figure 4c). Our map also highlights higher heat production values in West Antarctica. However, due to the thin crust in West Antarctica, the crustal contribution from this region averages 20 mW/m^2. In some localized areas like AP, MBL, and Ellsworth Mountain, the contribution from crustal heat production can be as high as 50 mW/m^2.

In Antarctica, continental scale heat flow estimation usually assumes a laterally uniform crustal heat production value (e.g. 1 $\mu W/m^3$ at the upper crust (An et al., 2015b), or 2.5 $\mu W/m^3$ at the surface and exponentially decreasing to 8 km (Martos et al., 2017)). To illustrate the contribution of the spatially variable heat production to the total geothermal heat flow, we use a uniform 1 $\mu W/m^3$ as a reference heat flow model for comparison. We calculate the radiogenic crust heat flow contribution with a minimum (25th percentile), best fitting (mode, Figure 4c), and maximum heat production case (75th percentile). We then compare our model results with the reference model (1 uW/m^3). All models are calculated with the same upper crust thickness (Figure 4b).

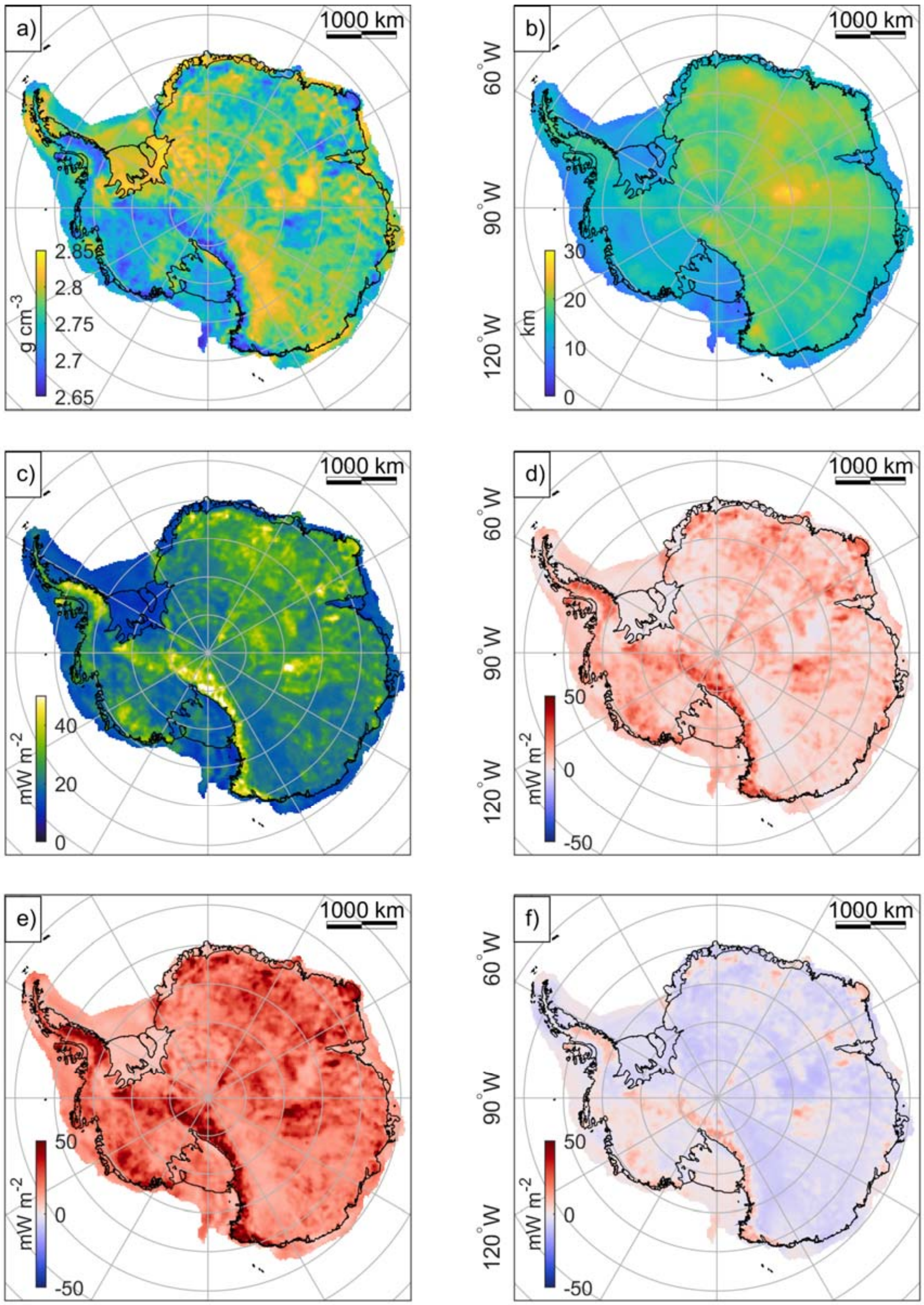

Figure 4. a) upper crust density; b) upper crust thickness; c) heat flow contribution due to crust heat production (based on mode fitting, 18 to 27 mW/m^2 from 25th to 75th percentile); d) heat flow variation (based on mode fitting) compared to uniform upper crust heat production at reference value (1μW/m^3); e) heat flow variation (based on 75th percentile fitting) compared to uniform upper crust heat production; f) heat flow variation (based on 25th percentile fitting) compared to uniform upper crust heat production.

The heat flow variation compared to the reference model is within 10 mW/m^2 for the most conservative heat production estimation (25th percentile fitting), with EANT showing negative variation and WANT a positive heat flow variation (Figure 4f). For mode case, the heat flow change is mostly positive, with an increase of 3.4 mW/m^2 at the 25th percentile and 9.5 mW/m^2 at the 75th percentile. For the maximum heat production case (75th percentile fitting, Figure 4e), areas including Antarctica Peninsula, Marie Byrd Land, TA, and the DML area show a positive heat flow variation up to 50 mW/m^2 above the reference.

Although our model exhibits significant variability depending on the chosen scenario, it is evident that, in all cases, highly variable heat flux is derived from radiogenic crust heat production variation. Further testing using different inversion densities (mean±STD) produces a similar pattern for elevated heat flow (Supporting Information Figure S10).

4.2.4 Implication for ice sheet system

GHF is a key boundary condition of the ice sheet flow as elevated heat flow warms the ice sheet bed, affecting ice rheology and potentially increasing basal melt rate (McCormack et al., 2022). Regions with higher GHF also lead to the formation of temperate ice, which in turn results in faster surface flow (Pittard et al., 2016). GHF also impacts ice sheet dynamic related subglacial hydrology. In areas where the basal temperature exceeds the pressure melting point, subglacial meltwater is generated, forming an input to the hydrological system. Based on numerical ice sheet modeling, the basal melting rate increases linearly with geothermal heat flow at a rate of approximately 0.1-0.4 mm/yr/(mW/m^2) (Joughin et al., 2009; Seroussi et al., 2017).

When considering the contribution of heat production to GHF, the model suggests a strong spatial variation in heat flow (ranging from 6-60 mW/m^2) due to the incorporation of variations in crustal heat production. Considering that mantle heat flow contributes to a long-wavelength heat source beneath the ice sheet, the short-wavelength heat source resulting from crustal heat production would result in a spatially heterogeneous basal melt (0.6-24 mm/yr). This spatial variability in basal conditions could be a crucial factor for the subglacial hydrology system and impact ice sheet dynamics.

5 Conclusions

We developed a crustal model for Antarctica using gravity inversion, constrained by seismic information. By analyzing the resulting crustal density and thickness, we generated a continental-scale crustal radiogenic heat production estimate and its contribution to spatially variable GHF (ranging from 6 to 60 mW/m^2). Our work provides critical information to capture the heterogeneity of the heat source beneath the ice sheet. This heterogeneity also provides new constraints for understanding the subglacial hydrology system and ice sheet dynamics.

Acknowledgments

This research was supported by the Australian Research Council Special Research Initiative, Australian Centre for Excellence in Antarctic Science (project number SR200100008). L.L. was supported by China Scholarship Council–The University of Western Australia joint PhD scholarship (201806170054).

Open Research

The model of Antarctic crustal structure and radiogenic heat production will be available in Zenodo repository [] and Github repository https://github.com/LL-Geo/ANT_Crust.

References

Abrehdary, M., & Sjöberg, L. (2021). Moho density contrast in Antarctica determined by satellite gravity and seismic models. *Geophysical Journal International*, *225*(3), 1952-1962.

Aitken, A. (2010). Moho geometry gravity inversion experiment (MoGGIE): a refined model of the Australian Moho, and its tectonic and isostatic implications. *Earth and Planetary Science Letters*, *297*(1-2), 71-83.

Aitken, A., Salmon, M., & Kennett, B. (2013). Australia's Moho: a test of the usefulness of gravity modelling for the determination of Moho depth. *Tectonophysics*, *609*, 468-479.

Aitken, A. R., Roberts, J. L., van Ommen, T. D., Young, D. A., Golledge, N. R., Greenbaum, J. S., Blankenship, D. D., & Siegert, M. J. (2016). Repeated large-scale retreat and advance of Totten Glacier indicated by inland bed erosion. *Nature*, *533*(7603), 385-389. https://doi.org/10.1038/nature17447

Alghamdi, A., Aitken, A., & Dentith, M. (2018). The deep crustal structure of the Warakurna LIP, and insights on Proterozoic LIP processes and mineralisation. *Gondwana Research*, *56*, 1-11.

An, M., Wiens, D. A., Zhao, Y., Feng, M., Nyblade, A. A., Kanao, M., Li, Y., Maggi, A., & Lévêque, J.-J. (2015a). S-velocity model and inferred Moho topography beneath the Antarctic Plate from Rayleigh waves. *Journal of Geophysical Research: Solid Earth*, *120*(1), 359-383. https://doi.org/10.1002/2014jb011332

An, M., Wiens, D. A., Zhao, Y., Feng, M., Nyblade, A. A., Kanao, M., Li, Y., Maggi, A., & Lévêque, J. J. (2015b). Temperature, lithosphere-asthenosphere boundary, and heat flux beneath the Antarctic Plate inferred from seismic velocities. *Journal of Geophysical Research: Solid Earth*, *120*(12), 8720-8742. https://doi.org/10.1002/2015jb011917

Baranov, A., & Morelli, A. (2013). The Moho depth map of the Antarctica region. *Tectonophysics*, *609*, 299-313. https://doi.org/10.1016/j.tecto.2012.12.023

Burton-Johnson, A., Halpin, J., Whittaker, J. M., Graham, F. S., & Watson, S. J. (2017). A new heat flux model for the Antarctic Peninsula incorporating spatially variable upper crustal radiogenic heat production. *Geophysical Research Letters*, *44*(11), 5436-5446.

Chaput, J., Aster, R. C., Huerta, A., Sun, X., Lloyd, A., Wiens, D., Nyblade, A., Anandakrishnan, S., Winberry, J. P., & Wilson, T. (2014). The crustal thickness of West Antarctica. *Journal of Geophysical Research: Solid Earth*, *119*(1), 378-395.

Chisenga, C., Yan, J., & Yan, P. (2019). A crustal thickness model of antactica calculated in spherical approximation from satellite gravimetric data. *Geophysical Journal International*. https://doi.org/10.1093/gji/ggz154

Dunham, C., O'Donnell, J., Stuart, G., Brisbourne, A., Rost, S., Jordan, T., Nyblade, A., Wiens, D., & Aster, R. (2020). A joint inversion of receiver function and Rayleigh wave phase velocity dispersion data to estimate crustal structure in West Antarctica. *Geophysical Journal International*, *223*(3), 1644-1657.

Ferraccioli, F., Finn, C. A., Jordan, T. A., Bell, R. E., Anderson, L. M., & Damaske, D. (2011). East Antarctic rifting triggers uplift of the Gamburtsev Mountains. *Nature*, *479*(7373), 388-392. https://doi.org/10.1038/nature10566

Frederick, B. C., Young, D. A., Blankenship, D. D., Richter, T. G., Kempf, S. D., Ferraccioli, F., & Siegert, M. J. (2016). Distribution of subglacial sediments across the Wilkes Subglacial Basin, East Antarctica. *Journal of Geophysical Research: Earth Surface*, *121*(4), 790-813. https://doi.org/doi:10.1002/2015JF003760

Fullagar, P. K., Pears, G. A., & McMonnies, B. (2008). Constrained inversion of geologic surfaces—Pushing the boundaries. *The Leading Edge*, *27*(1), 98-105.

Gard, M., Hasterok, D., & Halpin, J. A. (2019). Global whole-rock geochemical database compilation. *Earth System Science Data*, *11*(4), 1553-1566.

Golynsky, A., Chiappini, M., Damaske, D., Ferraccioli, F., Finn, C. A., Ishihara, T., Kim, H. R., Kovacs, L., Masolov, V. N., & Morris, P. (2006). ADMAP—A digital magnetic anomaly map of the Antarctic. In *Antarctica* (pp. 109-116). Springer.
Haeger, C., & Kaban, M. K. (2019). Decompensative Gravity Anomalies Reveal the Structure of the Upper Crust of Antarctica. *Pure and Applied Geophysics*. https://doi.org/10.1007/s00024-019-02212-5
Haeger, C., Kaban, M. K., Tesauro, M., Petrunin, A. G., & Mooney, W. D. (2019). 3D density, thermal and compositional model of the Antarctic lithosphere and implications for its evolution. *Geochemistry, Geophysics, Geosystems*, *0*. https://doi.org/doi:10.1029/2018GC008033
Hansen, S. E., Julià, J., Nyblade, A. A., Pyle, M. L., Wiens, D. A., & Anandakrishnan, S. (2009). Using S wave receiver functions to estimate crustal structure beneath ice sheets: An application to the Transantarctic Mountains and East Antarctic craton. *Geochemistry Geophysics Geosystems*, *10*, Q08014. https://doi.org/10.1029/2009gc002576
Hansen, S. E., Nyblade, A. A., Heeszel, D. S., Wiens, D. A., Shore, P., & Kanao, M. (2010). Crustal structure of the Gamburtsev Mountains, East Antarctica, from S-wave receiver functions and Rayleigh wave phase velocities. *Earth and Planetary Science Letters*, *300*(3-4), 395-401. https://doi.org/10.1016/j.epsl.2010.10.022
Joughin, I., Tulaczyk, S., Bamber, J. L., Blankenship, D., Holt, J. W., Scambos, T., & Vaughan, D. G. (2009). Basal conditions for Pine Island and Thwaites Glaciers, West Antarctica, determined using satellite and airborne data. *Journal of Glaciology*, *55*(190), 245-257.
Kvas, A., Mayer-Gürr, T., Krauss, S., Brockmann, J. M., Schubert, T. S., Wolf-Dieter;, Pail, R. G., Thomas;, Jäggi, A., & Meyer, U. (2019). *The satellite-only gravity field model GOCO06s*. https://doi.org/ http://doi.org/10.5880/ICGEM.2019.002
Li, L., Aitken, A. R., Lindsay, M. D., & Kulessa, B. (2022). Sedimentary basins reduce stability of Antarctic ice streams through groundwater feedbacks. *Nature Geoscience*, *15*, 645-650.
Lloyd, A. J., Wiens, D. A., Zhu, H., Tromp, J., Nyblade, A. A., Aster, R. C., Hansen, S. E., Dalziel, I. W., Wilson, T. J., & Ivins, E. R. (2020). Seismic structure of the Antarctic upper mantle imaged with adjoint tomography. *Journal of Geophysical Research: Solid Earth*, *125*(3).
Llubes, M., Seoane, L., Bruinsma, S., & Rémy, F. (2018). Crustal thickness of Antarctica estimated using data from gravimetric satellites. *Solid Earth*, *9*(2), 457-467. https://doi.org/10.5194/se-9-457-2018
Maritati, A., Aitken, A. R. A., Young, D. A., Roberts, J. L., Blankenship, D. D., & Siegert, M. J. (2016). The tectonic development and erosion of the Knox Subglacial Sedimentary Basin, East Antarctica. *Geophysical Research Letters*, *43*(20), 10,728-710,737. https://doi.org/10.1002/2016gl071063
Martos, Y. M., Catalán, M., Jordan, T. A., Golynsky, A., Golynsky, D., Eagles, G., & Vaughan, D. G. (2017). Heat Flux Distribution of Antarctica Unveiled. *Geophysical Research Letters*, *44*(22), 11,417-411,426. https://doi.org/10.1002/2017gl075609
McCormack, F. S., Roberts, J. L., Dow, C. F., Stål, T., Halpin, J. A., Reading, A. M., & Siegert, M. J. (2022). Fine-scale geothermal heat flow in Antarctica can increase simulated subglacial melt estimates. *Geophysical Research Letters*, e2022GL098539.
Morlighem, M., Rignot, E., Binder, T., Blankenship, D., Drews, R., Eagles, G., Eisen, O., Ferraccioli, F., Forsberg, R., Fretwell, P., Goel, V., Greenbaum, J. S., Gudmundsson, H., Guo, J., Helm, V., Hofstede, C., Howat, I., Humbert, A., Jokat, W., . . . Young, D. A. (2020). Deep glacial troughs and stabilizing ridges unveiled beneath the margins of the Antarctic ice sheet. *Nature Geoscience*, *13*(2), 132-137. https://doi.org/10.1038/s41561-019-0510-8
Noble, T. L., Rohling, E. J., Aitken, A. R. A., Bostock, H. C., Chase, Z., Gomez, N., Jong, L. M., King, M. A., Mackintosh, A. N., McCormack, F. S., McKay, R. M., Menviel, L., Phipps, S. J., Weber, M. E., Fogwill, C. J., Gayen, B., Golledge, N. R., Gwyther, D. E., Hogg, A. M., . . . Williams, T. (2020). The Sensitivity of the Antarctic Ice Sheet to a Changing Climate: Past, Present, and Future. *Reviews of Geophysics*, *58*(4). https://doi.org/10.1029/2019RG000663
Pappa, F., Ebbing, J., & Ferraccioli, F. (2019a). Moho Depths of Antarctica: Comparison of Seismic, Gravity, and Isostatic Results. *Geochemistry, Geophysics, Geosystems*. https://doi.org/10.1029/2018gc008111
Pappa, F., Ebbing, J., Ferraccioli, F., & van der Wal, W. (2019b). Modeling satellite gravity gradient data to derive density, temperature, and viscosity structure of the Antarctic lithosphere. *Journal of Geophysical Research: Solid Earth*, *124*(11), 12053-12076.
Pittard, M., Roberts, J., Galton-Fenzi, B., & Watson, C. (2016). Sensitivity of the Lambert-Amery glacial system to geothermal heat flux. *Annals of Glaciology*, *57*(73), 56-68.

Reading, A. M., Stål, T., Halpin, J. A., Lösing, M., Ebbing, J., Shen, W., McCormack, F. S., Siddoway, C. S., & Hasterok, D. (2022). Antarctic geothermal heat flow and its implications for tectonics and ice sheets. *Nature Reviews Earth & Environment*. https://doi.org/10.1038/s43017-022-00348-y

Sanchez, G., Halpin, J. A., Gard, M., Hasterok, D., Staal, T., Raimondo, T., Peters, S., & Burton-Johnson, A. (2021). PetroChron Antarctica: A geological database for interdisciplinary use. *Geochemistry, Geophysics, Geosystems*, *22*(12), e2021GC010154.

Scheinert, M., Ferraccioli, F., Schwabe, J., Bell, R., Studinger, M., Damaske, D., Jokat, W., Aleshkova, N., Jordan, T., Leitchenkov, G., Blankenship, D. D., Damiani, T. M., Young, D., Cochran, J. R., & Richter, T. D. (2016). New Antarctic Gravity Anomaly Grid for Enhanced Geodetic and Geophysical Studies in Antarctica. *Geophysical Research Letters*, *43*(2), 600-610. https://doi.org/10.1002/2015GL067439

Seroussi, H., Ivins, E. R., Wiens, D. A., & Bondzio, J. (2017). Influence of a West Antarctic mantle plume on ice sheet basal conditions. *Journal of Geophysical Research: Solid Earth*, *122*(9), 7127-7155.

Shen, W., Wiens, D., Anandakrishnan, S., Aster, R., Gerstoft, P., Bromirski, P., Hansen, S. E., Dalziel, I. W. D., Heeszel, D. S., Huerta, A. D., Nyblade, A. A., Stephen, R., Wilson, T. J., & Winberry, J. P. (2018). The Crust and Upper Mantle Structure of Central and West Antarctica From Bayesian Inversion of Rayleigh Wave and Receiver Functions. *Journal of Geophysical Research-Solid Earth*, *123*(9), 7824-7849. https://doi.org/10.1029/2017jb015346

Straume, E. O., Gaina, C., Medvedev, S., Hochmuth, K., Gohl, K., Whittaker, J. M., Abdul Fattah, R., Doornenbal, J. C., & Hopper, J. R. (2019). GlobSed: Updated Total Sediment Thickness in the World's Oceans. *Geochemistry, Geophysics, Geosystems*, *20*, 1756– 1772. https://doi.org/10.1029/2018gc008115

Tankersley, M. D., Horgan, H. J., Siddoway, C. S., Tontini, F. C., & Tinto, K. J. (2022). Basement topography and sediment thickness beneath Antarctica’s Ross Ice Shelf. *Geophysical Research Letters*, e2021GL097371.

Zhang, C., von Frese, R. R., Shum, C., Leftwich, T. E., Kim, H. R., & Golynsky, A. V. (2020). Satellite Gravity Constraints on the Antarctic Moho and Its Potential Isostatic Adjustments. *Geochemistry, Geophysics, Geosystems*, *21*(12), e2020GC009048.

Zhou, Z., Wiens, D. A., Shen, W., Aster, R. C., Nyblade, A., & Wilson, T. J. (2022). Radial Anisotropy and sediment thickness of West and Central Antarctica estimated from Rayleigh and Love wave velocities. *Journal of Geophysical Research: Solid Earth*, *127*(3), e2021JB022857.